Ultrasensitive detection of malignant melanoma using PET molecular imaging probes

Ayoung Pyo[a,b,c], Dong-Yeon Kim[a,b,c,1], Heejung Kim[d], Daejin Lim[e], Seong Young Kwon[a,b,c], Sae-Ryung Kang[a,b,c], Hyung-Seok Kim[f], Hee-Seung Bom[a,b,c], and Jung-Joon Min[a,b,c,1]

[a]Department of Nuclear Medicine, Chonnam National University Medical School and Hwasun Hospital, 58128 Hwasun, Korea; [b]Institute for Molecular Imaging and Theranostics, Chonnam National University Medical School, 58128 Hwasun, Korea; [c]Innovation Center for Molecular Probe Development, Chonnam National University Hwasun Hospital, 58128 Hwasun, Korea; [d]Korea Drug Development Platform using Radioisotope, Korea Institute of Radiological & Medical Sciences, 01812 Seoul, Korea; [e]Department of Microbiology, Chonnam National University Medical School, 58128 Hwasun, Korea; and [f]Department of Forensic Medicine, Chonnam National University Medical School, 58128 Hwasun, Korea

Edited by Michael E. Phelps, David Geffen School of Medicine at University of California, Los Angeles, CA, and approved April 21, 2020 (received for review December 18, 2019)

Malignant melanoma has one of the highest mortality rates of any cancer because of its aggressive nature and high metastatic potential. Clinical staging of the disease at the time of diagnosis is very important for the prognosis and outcome of melanoma treatment. In this study, we designed and synthesized the ^{18}F-labeled pyridine-based benzamide derivatives *N*-(2-(dimethylamino)ethyl)-5-[^{18}F]fluoropicolinamide ([^{18}F]DMPY2) and *N*-(2-(dimethylamino)ethyl)-6-[^{18}F]fluoronicotinamide ([^{18}F]DMPY3) to detect primary and metastatic melanoma at an early stage and evaluated their performance in this task. [^{18}F]DMPY2 and [^{18}F]DMPY3 were synthesized by direct radiofluorination of the bromo precursor, and radiochemical yields were ∼15–20%. Cell uptakes of [^{18}F]DMPY2 and [^{18}F]DMPY3 were >103-fold and 18-fold higher, respectively, in B16F10 (mouse melanoma) cells than in negative control cells. Biodistribution studies revealed strong tumor uptake and retention of [^{18}F]DMPY2 (24.8% injected dose per gram of tissue [ID/g] at 60 min) and [^{18}F]DMPY3 (11.7%ID/g at 60 min) in B16F10 xenografts. MicroPET imaging of both agents demonstrated strong tumoral uptake/retention and rapid washout, resulting in excellent tumor-to-background contrast in B16F10 xenografts. In particular, [^{18}F]DMPY2 clearly visualized almost all metastatic lesions in lung and lymph nodes, with excellent image quality. [^{18}F]DMPY2 demonstrated a significantly higher tumor-to-liver ratio than [^{18}F]fluorodeoxyglucose ([^{18}F]FDG) and the previously reported benzamide tracers *N*-[2-(diethylamino)-ethyl]-5-[^{18}F]fluoropicolinamide ([^{18}F]P3BZA) and *N*-[2-(diethylamino)-ethyl]-4-[^{18}F]fluorobenzamide ([^{18}F]FBZA) in B16F10-bearing or SK-MEL-3 (human melanoma)-bearing mice. In conclusion, [^{18}F]DMPY2 might have strong potential for the diagnosis of early stage primary and metastatic melanoma using positron emission tomography (PET).

malignant melanoma | metastasis | ^{18}F-labeled pyridine-based benzamide derivative | PET | molecular imaging

Malignant melanoma derived from melanocytes is the most aggressive type and deadliest form of skin cancer, with the highest rates of metastasis and mortality (1, 2). The incidence of metastatic melanoma has rapidly increased over the past three decades (3). In the last few years, new therapeutic strategies, targeted therapies, and immunotherapy have been developed for melanoma, and these have improved the patient's prognosis.

With the emergence of new therapeutic modalities, the diagnosis of melanoma at the earliest practicable stage has become more important for improving the survival of patients (4). Positron emission tomography (PET) can visualize specific molecular pathways or biomarkers of the disease process and offers the promise of noninvasively imaging micrometastases (5, 6). However, PET must be coupled with an appropriate imaging probe to provide highly sensitive detection of metastases and accurate staging of high-risk melanomas. Although several PET probes, including [^{18}F]fluorodeoxyglucose ([^{18}F]FDG), L-6-[^{18}F]fluoro-3,4-dihydroxyphenylalanine ([^{18}F]FDOPA), 2-amino-4-[^{11}C]methylsulfanyl-butanoic acid ([^{11}C]methionine), 3′-[^{18}F]fluoro-3′-deoxythymidine ([^{18}F]FLT), and [^{18}F]galacto-RGD peptide have been evaluated for melanoma detection, only [^{18}F]FDG is currently used in the clinic (7–11). However, [^{18}F]FDG PET/computed tomography (CT) has shown very low detection rates for occult metastatic lesions in patients (12) and has often failed to identify metastatic lesions smaller than 1 cm in diameter located in the common metastatic sites of the lungs, liver, and brain (5). Therefore, novel PET probes with excellent in vivo performance for melanoma are highly desired for the detection of small lesions and metastases.

Many kinds of molecular probes have been designed and evaluated for melanoma detection, including antibody-based imaging agents (13, 14), melanocortin-1 receptor targeting probes (15–17), α-melanocyte stimulating hormone derivatives (18–20), and benzamide derivatives (21–24). Among these, benzamide derivatives have been actively investigated and shown to be among the most promising for melanoma detection (4). Benzamide analogs have a selective affinity for melanin, the formation of which is highly increased in malignant melanoma because of the elevated tyrosinase activity, a rate-limiting enzyme in the biosynthesis of melanin. ^{123}I-labeled benzamide

Significance

With the emergence of new therapeutic modalities, the diagnosis of melanoma at the earliest practicable stage has become more important for improving the survival of patients. We developed a positron emission tomography (PET) imaging probe, *N*-(2-(dimethylamino)ethyl)-5-[^{18}F]fluoropicolinamide ([^{18}F]DMPY2) and evaluated diagnostic performance in animal models. [^{18}F]DMPY2 PET exhibited excellent performance in detecting primary and metastatic melanomas, demonstrating strong/prolonged tumoral uptake and rapid background clearance. This suggests that this radiotracer could be used as a novel PET imaging agent to obtain outstanding image quality in the diagnosis of melanoma. This is the pioneering report of pyridine-based benzamide derivative with reduced alkyl chains in the amine residue and ultrasensitive detection of melanoma lesions in living subjects compared to conventional PET imaging agents.

Author contributions: D.-Y.K. and J.-J.M. designed research; A.P., D.-Y.K., H.K., and D.L. performed research; A.P., D.-Y.K., S.Y.K., S.-R.K., H.-S.K., and H.-S.B. analyzed data; and A.P., D.-Y.K., and J.-J.M. wrote the paper.

The authors declare no competing interest.

This article is a PNAS Direct Submission.

[1]To whom correspondence may be addressed. Email: blueburr@gmail.com or jjmin@jnu.ac.kr.

This article contains supporting information online at https://www.pnas.org/lookup/suppl/doi:10.1073/pnas.1922313117/-/DCSupplemental.

First published May 21, 2020.

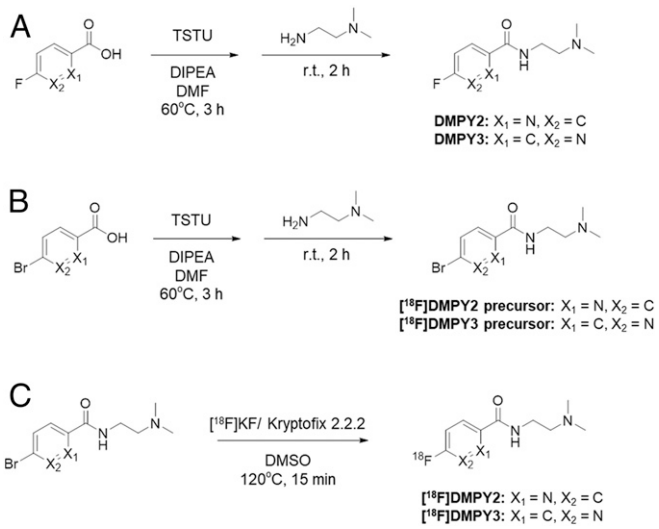

Fig. 1. Chemical structure and synthesis scheme of the reference compounds, precursors, and radiotracers. (*A*) Synthesis scheme of DMPY2 and DMPY3. DMPY2 and DMPY3 were synthesized via a one-pot reaction. The synthesis yields of DMPY2 and DMPY3 were 89.19 ± 3.26% and 85.83 ± 7.59%, respectively ($n = 3$). (*B*) Synthesis scheme of the precursors for each radiotracer. Bromide was introduced as the leaving group for the radiosynthesis. The precursors showed similar chemical yields to the reference compounds ([^{18}F]DMPY2 precursor: 88.56 ± 6.15%, $n = 5$; [^{18}F]DMPY3 precursor: 86.55 ± 4.11%, $n = 4$). (*C*) Radiosynthesis of [^{18}F]DMPY2 and [^{18}F]DMPY3. Radiotracers were synthesized via a simple one-step nucleophilic substitution reaction. The radiochemical yields of [^{18}F]DMPY2 and [^{18}F]DMPY3 were 19.32 ± 4.78% and 18.92 ± 5.55%, respectively ($n > 20$), and the specific activity of each tracer was > 7.6 GBq/μmol.

derivatives and ^{99m}Tc-labeled benzamide derivatives have been investigated for melanoma detection (25–31). In recent years, ^{68}Ga- or ^{18}F-labeled benzamide derivative PET imaging agents, which provide higher spatial resolution, have also been reported (21–24, 32–37).

Benzamide derivatives have a chemical structure consisting of three parts: a benzamide, an aliphatic linker, and an amine residue. Each part of the chemical structure has been modified to improve the radiochemical yield (RCY), melanin binding affinity, and pharmacokinetic properties in animal models. First, pyridine-based benzamide derivatives have shown higher uptake values than benzene-based benzamide derivatives in B16F10 tumor-bearing mice (4). The pyridine-based agent *N*-(2-(diethylamino)-ethyl)-5-[^{18}F]fluoropicolinamide ([^{18}F]P3BZA) was evaluated in melanoma patients in a preliminary clinical application, and its potential for use in melanoma diagnosis was suggested (35). Second, an amine residue has been modified because melanin can bind to aliphatic-only structures such as *N,N*-diethylethylenediamine (38). In this regard, we recently reported on the novel benzamide derivative *N*-(2-(dimethylamino)ethyl)-4-[^{18}F]fluorobenzamide ([^{18}F]DMFB), which has a carbon chain amine residue in the benzamide derivative shortened from diethyl to dimethyl. [^{18}F]DMFB has improved in vivo performance for the detection of melanoma and its metastases (39).

In this study, we introduce two ^{18}F-labeled pyridine-based benzamide derivatives with a dimethyl amine residue: *N*-(2-(dimethylamino)ethyl)-5-[^{18}F]fluoropicolinamide ([^{18}F]DMPY2) and *N*-(2-(dimethylamino)ethyl)-6-[^{18}F]fluoronicotinamide ([^{18}F]DMPY3). We characterize these two derivatives for the early detection of primary or metastatic melanoma and demonstrate excellent quality imaging for the detection of lesions, superior to that obtained with [^{18}F]FDG and the other ^{18}F-labeled benzamide derivatives [^{18}F]P3BZA and *N*-[2-(diethylamino)-ethyl]-4-[^{18}F]fluorobenzamide ([^{18}F]FBZA) (4, 23).

Results

Tracer Preparation, In Vitro and In Vivo Stability, and Partition Coefficient. The structures and synthetic schemes of the precursors [^{18}F/^{19}F]DMPY2 and [^{18}F/^{19}F]DMPY3 are shown in Fig. 1. DMPY2 and DMPY3 were synthesized via one-step procedures between 5-fluoropicolinic acid or 6-fluoronicotinic acid and *N,N*-dimethylethylenediamine. Silica gel chromatography was used for separation, and the structural identity was analyzed by ^{1}H, ^{13}C NMR, and high-resolution mass spectrometry (*SI Appendix*,

Table 1. Biodistribution and tumor-to-organ (lung, liver, intestine, bone, brain, and skin) ratios of [^{18}F]DMPY2 and [^{18}F]DMPY3 at 10, 30, and 60 min after i.v. injection ($n = 3$ per time point) in Foxn1nu mice bearing B16F10 tumors

	[^{18}F]DMPY2			[^{18}F]DMPY3		
Organ	10 min	30 min	60 min	10 min	30 min	60 min
Blood	5.34 ± 0.97	2.64 ± 0.81	2.10 ± 0.37	4.60 ± 0.73	3.30 ± 0.50	1.13 ± 0.17
Heart	6.06 ± 0.79	2.43 ± 0.47	1.99 ± 0.37	5.21 ± 0.54	3.43 ± 0.41	1.42 ± 0.27
Lung	12.38 ± 2.86	3.93 ± 1.60	3.09 ± 0.67	9.01 ± 0.99	6.71 ± 0.75	2.77 ± 0.35
Liver	12.23 ± 2.31	3.53 ± 1.15	3.41 ± 0.45	17.95 ± 4.75	7.60 ± 0.57	2.47 ± 0.86
Spleen	19.30 ± 3.64	4.58 ± 2.34	3.61 ± 1.15	12.66 ± 2.04	8.20 ± 1.56	2.19 ± 0.12
Stomach	11.15 ± 3.20	7.65 ± 0.79	12.28 ± 1.99	3.24 ± 0.61	4.97 ± 2.35	1.57 ± 0.73
Intestine	14.25 ± 5.24	5.15 ± 2.03	4.05 ± 1.25	12.92 ± 3.83	8.00 ± 1.67	2.64 ± 0.00
Kidney	31.55 ± 8.97	17.00 ± 4.58	10.06 ± 2.73	39.04 ± 15.20	15.56 ± 2.68	5.97 ± 2.07
Pancreas	12.92 ± 3.51	3.44 ± 0.98	2.40 ± 0.42	10.64 ± 2.72	3.84 ± 0.68	1.75 ± 0.28
Muscle	4.66 ± 0.44	2.81 ± 1.12	2.49 ± 0.94	5.46 ± 0.76	3.69 ± 0.76	2.21 ± 1.09
Bone	5.32 ± 1.26	2.05 ± 0.66	2.68 ± 1.40	4.48 ± 1.72	2.43 ± 0.29	1.88 ± 0.39
Brain	11.05 ± 4.23	2.43 ± 0.98	1.59 ± 0.49	2.74 ± 0.67	2.16 ± 0.59	1.98 ± 0.39
Skin	6.91 ± 2.31	3.51 ± 0.74	4.20 ± 1.15	4.20 ± 0.89	4.63 ± 0.55	2.58 ± 0.61
Eyes	4.10 ± 1.55	2.17 ± 0.57	2.00 ± 0.26	3.31 ± 0.53	2.23 ± 0.51	1.39 ± 0.36
Tumor	9.20 ± 2.32	15.75 ± 5.62	24.86 ± 2.30	8.32 ± 1.30	9.83 ± 1.70	11.69 ± 2.74
Tumor-to-lung	0.74 ± 0.11	5.05 ± 4.19	8.37 ± 2.30	0.93 ± 0.14	1.48 ± 0.32	4.20 ± 0.69
Tumor-to-liver	0.77 ± 0.24	5.07 ± 3.39	7.42 ± 1.52	0.49 ± 0.16	1.31 ± 0.32	5.23 ± 2.32
Tumor-to-intestine	0.66 ± 0.09	3.35 ± 1.70	6.59 ± 2.23	0.68 ± 0.21	1.27 ± 0.35	4.43 ± 1.04
Tumor-to-bone	1.86 ± 0.87	8.61 ± 5.52	10.67 ± 4.06	2.13 ± 1.06	4.03 ± 0.21	6.61 ± 2.93
Tumor-to-brain	0.87 ± 0.24	8.45 ± 7.31	16.46 ± 4.38	3.08 ± 0.28	4.77 ± 1.49	6.29 ± 2.86
Tumor-to-skin	1.41 ± 0.56	4.82 ± 2.59	6.31 ± 2.19	2.00 ± 0.12	2.12 ± 0.30	4.89 ± 2.33

Figs. S1–S4). The chemical yields of DMPY2 and DMPY3 were 80–85%. Differing from cold synthesis, [^{18}F]DMPY2 and [^{18}F]DMPY3 were synthesized via one-step nucleophilic substitution reactions of no-carrier-added [^{18}F]fluoride with the bromo precursors 5-bromo-*N*-(2-(dimethylamino)ethyl)picolinamide or 6-bromo-*N*-(2-(dimethylamino)ethyl)nicotinamide in the presence of Kryptofix 2.2.2 and K_2CO_3. The total synthesis time for the [^{18}F]DMPY2 or [^{18}F]DMPY3 was within 50 min, including separation using HPLC (high-performance liquid chromatography). The overall decay-corrected RCYs of [^{18}F]DMPY2 and [^{18}F]DMPY3 were ∼15–20%. The identity of [^{18}F]DMPY2 and [^{18}F]DMPY3 were confirmed by comparing their retention times with that of the reference compound (*SI Appendix*, Figs. S8 and S9). The specific activity of the tracers was greater than 7.6 GBq/μmol. When the radiotracers were incubated in human serum at 37 °C for 2 h, the percentage of the remaining radiotracers (R_f, 0.15–0.20) was greater than 95%. No metabolite was detected in the serum of mice 60 and 120 min after intravenous (i.v.) injection of [^{18}F]DMPY2 (98.40 ± 0.86% and 98.26 ± 0.90%, $n = 4$, respectively; *SI Appendix*, Fig. S12).

[^{18}F/^{19}F]P3BZA and [^{18}F/^{19}F]FBZA were synthesized following previous publications (4, 23). The structural identity of [^{18}F/^{19}F]P3BZA and [^{18}F/^{19}F]FBZA was confirmed by ^{1}H and ^{13}C NMR (*SI Appendix*, Figs. S5–S7) and HPLC comparisons of ^{18}F-labeled compounds with the reference compounds (*SI Appendix*, Figs. S10 and S11).

The lipophilicity of the benzamide tracers was measured; the log *P* values of [^{18}F]DMPY2, [^{18}F]DMPY3, [^{18}F]P3BZA, and [^{18}F]FBZA were −2.63 ± 0.01, −1.76 ± 0.01, −2.08 ± 0.02, and −1.03 ± 0.01, respectively (*SI Appendix*, Table S2).

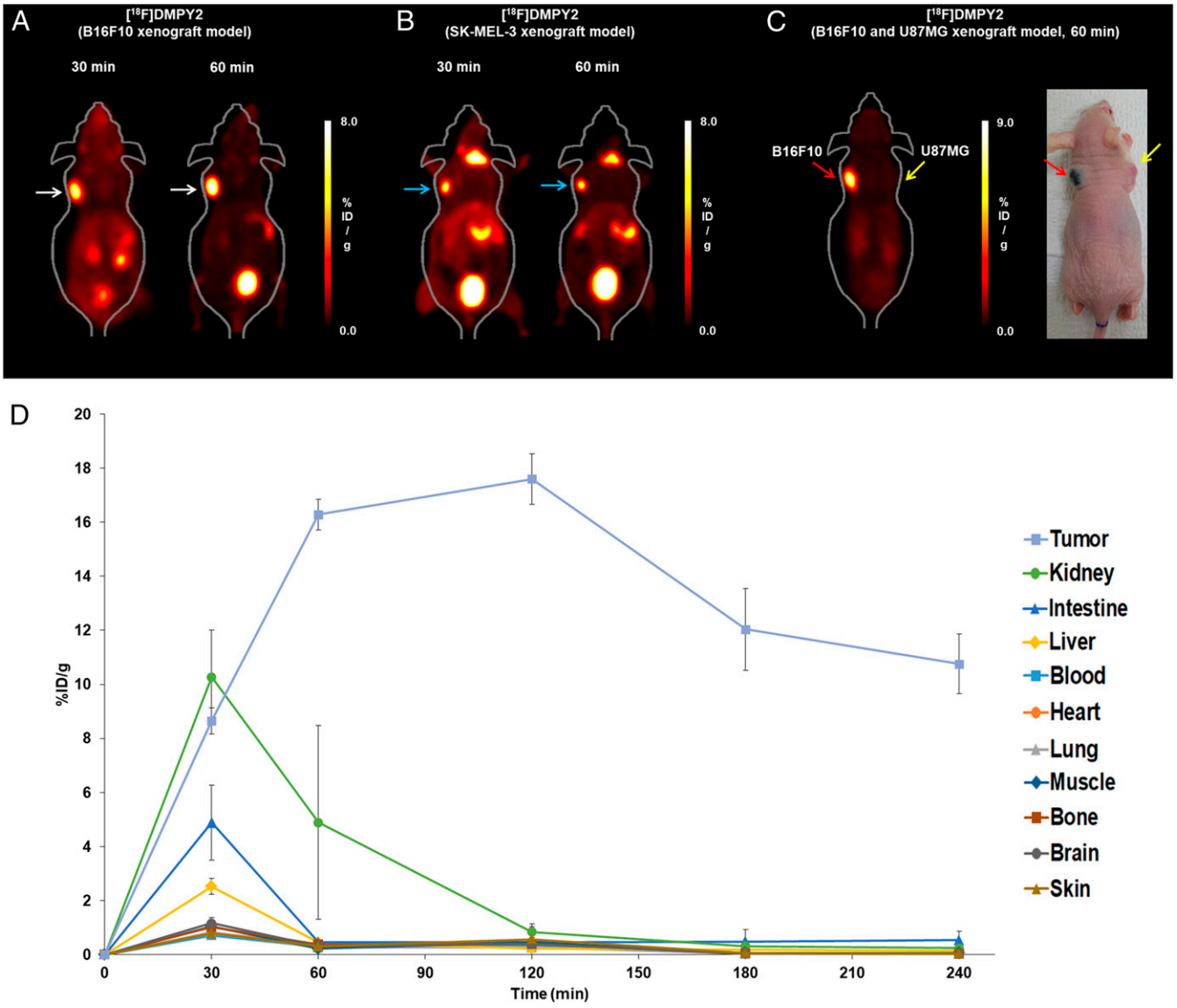

Fig. 2. MicroPET assessment of [^{18}F]DMPY2 in tumor-bearing models. Representative microPET images of mice bearing B16F10 (white arrow) (*A*) and SK-MEL-3 (blue arrow) (*B*) tumors at 30 and 60 min after injection of [^{18}F]DMPY2 ($n = 5$). (*C*) MicroPET image and photograph of a mouse bearing two different types of tumor (red arrow, B16F10; yellow arrow, U87MG) at 60 min postinjection of [^{18}F]DMPY2. (*D*) Time-activity curve of [^{18}F]DMPY2 in B16F10 tumors and several organs and tissues such as blood, heart, lung, liver, intestine, kidney, muscle, bone, brain, and skin, from 0 to 4 h postinjection ($n = 4$–12, *SI Appendix*, Table S1). Foxn1nu mice (5–6 wk old) were injected in the shoulder with B16F10 cells (1×10^6), SK-MEL-3 cells (3×10^6), and/or U87MG cells (1×10^7). MicroPET studies of the tumor models (tumor size: 80–120 mm^3) were performed after i.v. injection of [^{18}F]DMPY2 (7.4 MBq), with the images being acquired for 10 min.

In Vitro Cellular Uptake Study of [^{18}F]DMPY2 and [^{18}F]DMPY3. Cellular uptake values for [^{18}F]DMPY2 and [^{18}F]DMPY3 in the B16F10 cell line are shown in *SI Appendix*, Fig. S13. Treatment with L-tyrosine (2 mM) stimulated the B16F10 cells and changed their color to black, with these black cells then being considered as "activated" melanoma cells. Importantly, specific accumulation was observed with both tracers. The uptake of [^{18}F]DMPY2 and [^{18}F]DMPY3 increased from 2.14 ± 0.29% and 0.50 ± 0.10%, respectively, at 10 min to 3.11 ± 0.26% and 2.39 ± 0.46%, respectively, at 1 h. The uptake of [^{18}F]DMPY2 was more than 163-fold higher in activated B16F10 cells than in nonactivated cells at 10 min after treatment ($P < 0.05$), while [^{18}F]DMPY3 showed 58-fold higher uptake values in activated cells than in nonactivated cells at 1 h after treatment ($P < 0.05$). Overall, these results suggest that [^{18}F]DMPY2 can target melanin more efficiently and quickly than [^{18}F]DMPY3.

In Vivo Biodistribution Study of [^{18}F]DMPY2 and [^{18}F]DMPY3. The in vivo biodistribution study was performed in B16F10 tumor-bearing Foxn1nu mice at 10, 30, and 60 min post-i.v. injection of [^{18}F]DMPY2 or [^{18}F]DMPY3 (Table 1). Both agents revealed high and rapid accumulation and prolonged retention in tumors. Tumor uptakes of [^{18}F]DMPY2 and [^{18}F]DMPY3 (expressed as the percentage injected dose per gram of tissue [%ID/g]) were 9.20 ± 2.32%ID/g and 8.32 ± 1.30%ID/g, respectively, at 10 min, nd 24.86 ± 2.30%ID/g and 11.69 ± 2.74%ID/g, respectively, at 1 h postradiotracer injection. Rapid clearance and low nonspecific binding in normal organs resulted in high tumor-to-lung, -liver, -intestine, -bone, -brain, and -skin ratios at 1 h ([^{18}F]DMPY2: 8.37 ± 2.30, 7.42 ± 1.52, 6.59 ± 2.23, 10.67 ± 4.06, 16.46 ± 4.38, and 6.31 ± 2.19, respectively; [^{18}F]DMPY3: 4.20 ± 0.69, 5.23 ± 2.32, 4.43 ± 1.04, 6.61 ± 2.93, 6.29 ± 2.86, and 4.89 ± 2.33, respectively).

MicroPET Imaging in Primary Tumor Models. MicroPET studies of [^{18}F]DMPY2 and [^{18}F]DMPY3 were performed in tumor-bearing Foxn1nu mice. B16F10 tumors were clearly visualized by both tracers at 30 min postinjection, with tumor uptake increasing for 1 h ([^{18}F]DMPY2: 8.65 ± 0.48%ID/g at 30 min, 16.28 ± 0.57%ID/g at 1 h; [^{18}F]DMPY3: 7.06 ± 1.01%ID/g at 30 min, 7.72 ± 0.86%ID/g at 1 h; Fig. 2*A*, *SI Appendix*, Fig. S16 and Table S1, and Movie S1), with excellent tumor-to-muscle contrast. Points of note are that there was no uptake in lung and liver after 30 min and that the tumor uptake value of [^{18}F]DMPY2 was significantly higher than that of [^{18}F]DMPY3 for all imaging time points (30 min: $P = 0.0087$, 60 min: $P = 0.0095$). Furthermore, [^{18}F]DMPY2 showed focal accumulation only in tumors, without any background activity at 2 h postinjection, and prolonged retention in tumors over a duration of 4 h (17.60 ± 0.94, 12.04 ± 1.52, and 10.76 ± 1.10%ID/g at 2, 3, and 4 h, respectively; Fig. 2*D* and *SI Appendix*, Fig. S14). This uptake pattern was reproduced in SK-MEL-3 human melanoma (moderate melanin expression) xenograft mouse models. [^{18}F]DMPY2 microPET also clearly visualized SK-MEL-3 tumors with excellent tumor-to-background ratios (6.34 ± 1.33%ID/g at 30 min, 7.98 ± 0.91%ID/g at 1 h; Fig. 2*B*). Only melanoma was specifically visualized when [^{18}F]DMPY2 microPET was performed on mice bearing dual tumors such as melanoma (B16F10, 11.17 ± 0.36%ID/g) and glioblastoma tumors (U87MG, 1.18 ± 0.32%ID/g; Fig. 2*C*). Tumor accumulation of [^{18}F]DMPY2 was dependent on the level of melanin expression, as indicated by lower accumulation of this tracer in xenografts of amelanotic human melanoma (A375-P, 0.81 ± 0.09%ID/g at 1 h; *SI Appendix*, Fig. S15).

MicroPET Imaging in Metastatic Melanomas. When microPET imaging was performed in lung metastasis models, the metastatic region was clearly visualized at 1 h after i.v. injection of [^{18}F]DMPY2 or [^{18}F]DMPY3. Representative maximum intensity projection (MIP) and axial images of normal mice and mice with lung metastases are presented in Fig. 3 ([^{18}F]DMPY2) and *SI Appendix*, Fig. S17 ([^{18}F]DMPY3). Region of interest (ROI) analysis showed that uptake of [^{18}F]DMPY2 in the lung metastasis model was 38.0 ± 1.08%ID/g ($n = 4$, $^*P < 0.05$), while that of [^{18}F]DMPY3 was 9.81 ± 1.74%ID/g ($n = 4$, $^*P < 0.05$). [^{18}F]DMPY2 uptake in lung metastasis was 115-fold higher than that in normal lung (normal lung uptake of [^{18}F]DMPY2: 0.33 ± 0.03%ID/g; Fig. 3*C*). More precise examination of lung metastasis using high-resolution autoradiography clearly demonstrated the specific uptake of [^{18}F]DMPY2 in melanin-containing micrometastases in lung, while there was virtually no signal in the unpigmented normal lung tissues (Fig. 3 *D* and *E*).

In addition to lung metastasis, we further evaluated the performance of [^{18}F]DMPY2 and [^{18}F]DMPY3 for detecting lymph node (LN) metastasis in mouse models. Eighteen days after direct injection of B16F10 cells into the foot pad, black-colored LN metastases had generated in the popliteal area (Fig. 4*A* and *SI Appendix*, Fig. S18*A*). As shown in Fig. 4*B* and *SI Appendix*, Fig. S18*B*, very small LN metastases (<2.0 mm) were clearly visualized by each tracer. [^{18}F]DMPY2 uptake in the LN metastases was higher than that of [^{18}F]DMPY3 (Fig. 4*C* and *SI Appendix*,

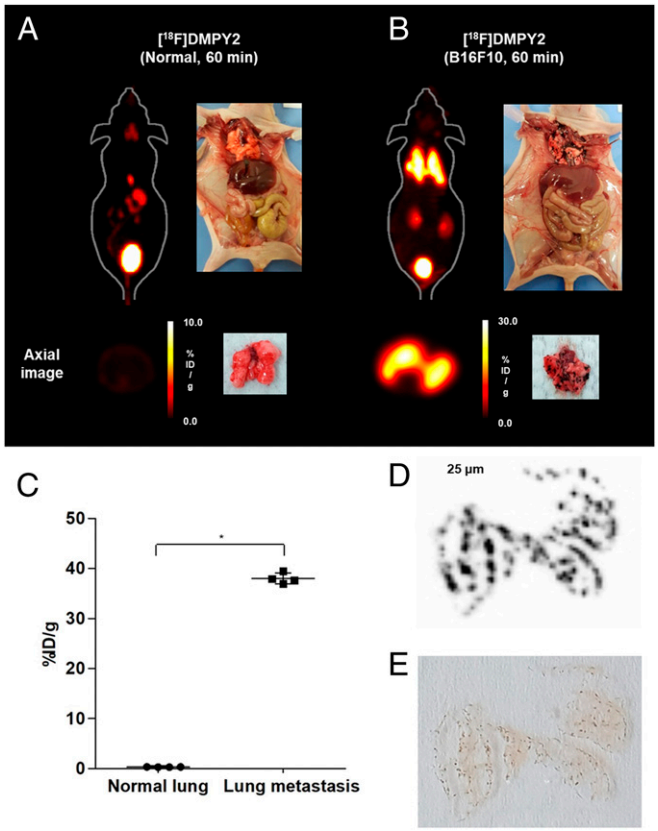

Fig. 3. Imaging assessment and analysis of [^{18}F]DMPY2 in lung metastasis models. Representative MIP (*Upper*) and transaxial (*Lower*) images (*Left*, PET; *Right*, Photograph) of a normal (*A*) and lung metastasis (*B*) model at 60 min postinjection of [^{18}F]DMPY2 ($n = 4$). The lung metastases were created in Foxn1nu mice via i.v. injection of B16F10 cells (2×10^5), and microPET studies were performed after 10 d (injection dose: 7.4 MBq, acquisition time: 10 min). (*C*) Quantitative analysis of [^{18}F]DMPY2 uptake in normal and metastatic lungs at 60 min ($n = 4$, $^*P < 0.05$). (*D*) Autoradiographic image of [^{18}F]DMPY2 and (*E*) photograph of metastatic lesions of a frozen lung section. Mice with B16F10 lung metastases were injected i.v. with 111 MBq of [^{18}F]DMPY2. After killing of the mice and removal of lungs, 25-μm frozen sections were cut using a cryostat.

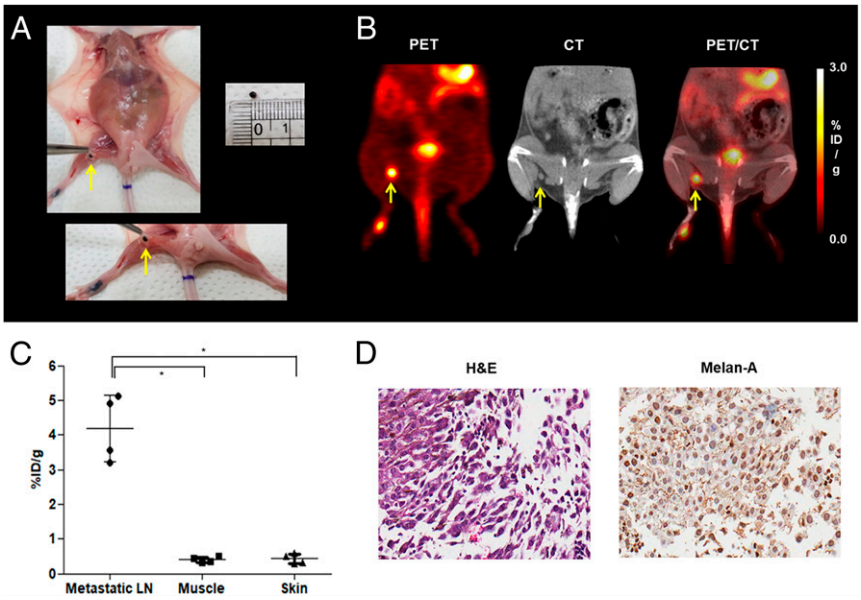

Fig. 4. [^{18}F]DMPY2 MicroPET/CT imaging and analysis in LN metastasis models. (*A*) Photograph of a representative B16F10 LN metastasis used in the MicroPET/CT studies. The LN metastasis models were generated by footpad injection of B16F10 cells (2×10^5 in 50 μL of Dulbecco's phosphate buffered saline) for 2 min ($n = 10$) into Foxn1nu mice. Different sized LN metastases (2–8 mm) were generated ($n = 10$). (*B*) MicroPET, CT, and PET/CT fusion images of a B16F10 LN metastasis model at 60 min after injection of [^{18}F]DMPY2 (yellow arrow: LN metastasis region). All LN metastases were successfully visualized by [^{18}F]DMPY2, regardless of the tumor size (*SI Appendix*, Fig. S16). (*C*) Quantitative analysis of [^{18}F]DMPY2 uptake in metastatic LNs, muscle, and skin at 60 min ($n = 4$, $^*P < 0.05$). (*D*) Pathological examination (H&E and Melan-A staining) of a metastatic LN.

Fig. S18*C*). All metastatic LNs (size range: 2–8 mm; $n = 10$) were successfully visualized by [^{18}F]DMPY2, regardless of tumor size (*SI Appendix*, Fig. S19). LN metastases were confirmed by histopathological analysis (Fig. 4*D* and *SI Appendix*, Fig. S18*D*).

Comparison of [^{18}F]DMPY2 with Conventional Radiotracers on MicroPET. We compared PET imaging using [^{18}F]DMPY2 and [^{18}F]DMPY3 with that using [^{18}F]FDG in B16F10 subcutaneous (s.c.) and lung metastasis models. All three radiotracers clearly visualized s.c. B16F10 tumors; however, they showed different biodistribution patterns (Fig. 5*A* and *SI Appendix*, Fig. S20). Radioactivity was specifically focused in tumors in [^{18}F]DMPY2 and [^{18}F]DMPY3 images, which showed extremely low background activity, whereas [^{18}F]FDG imaging showed uptake in several organs besides tumor, such as heart, liver, brain, and bladder. The tumor-to-lung, -liver, -intestine, -muscle, and -skin uptake ratios of [^{18}F]DMPY2 were 66.52 ± 21.78, 36.29 ± 3.55, 37.51 ± 8.69, 75.98 ± 15.66, and 57.30 ± 15.93, respectively, while the corresponding ratios for [^{18}F]FDG uptake were 9.32 ± 5.42, 4.44 ± 1.23, 1.91 ± 0.56, 12.99 ± 3.75, and 8.83 ± 3.59 ($n = 4$, $^*P < 0.05$, respectively; Fig. 5*C* and *SI Appendix*, Table S1). In the lung metastasis model, [^{18}F]DMPY2 exhibited clear uptake in the melanoma-bearing lung, whereas the high background activity of [^{18}F]FDG strongly impeded PET imaging (Fig. 5*B*). The tumor-to-liver, -intestine, -muscle, and -skin uptake ratios of [^{18}F]DMPY2 were 47.24 ± 13.54, 37.24 ± 12.95, 158.24 ± 52.00, and 99.15 ± 15.10, respectively, while the corresponding ratios for [^{18}F]FDG uptake were 1.39 ± 0.47, 0.91 ± 0.12, 4.84 ± 1.77, and 3.51 ± 0.84 ($n = 4$, $P < 0.05$, respectively; *SI Appendix*, Table S1).

Finally, we performed head-to-head comparisons between [^{18}F]DMPY2 and the other benzamide derivatives [^{18}F]P3BZA and [^{18}F]FBZA in Foxn1nu mice bearing B16F10 or SK-MEL-3 tumors. B16F10 tumors were visualized by all tracers at 1 h postinjection (Fig. 6*A*). Tumor uptake of [^{18}F]DMPY2 and [^{18}F]P3BZA was significantly higher than that of [^{18}F]FBZA ([^{18}F]DMPY2: 16.28 ± 0.57%ID/g; [^{18}F]P3BZA: 16.28 ± 5.58%ID/g; [^{18}F]FBZA: 10.74 ± 0.48%ID/g, $^*P < 0.05$; Fig. 6*B*). The tumor-to-liver ratio of [^{18}F]DMPY2 was over 11.0-fold and 14.7-fold higher than that of [^{18}F]P3BZA and [^{18}F]FBZA, respectively ([^{18}F]DMPY2: 36.29 ± 3.55; [^{18}F]P3BZA: 3.28 ± 1.34; [^{18}F]FBZA: 2.47 ± 0.24; $^*P < 0.05$; Fig. 6*C*). This uptake pattern was reproduced in an SK-MEL-3 human melanoma xenograft Foxn1nu mouse model. SK-MEL-3 tumors were also visualized by all tracers (Fig. 6*D*), and tumor uptake of [^{18}F]DMPY2 and [^{18}F]P3BZA was significantly higher than that of [^{18}F]FBZA at 1 h postinjection ([^{18}F]DMPY2: 7.98 ± 0.91%ID/g; [^{18}F]P3BZA: 11.23 ± 1.72%ID/g; [^{18}F]FBZA: 5.53 ± 0.55%ID/g; $^*P < 0.05$; Fig. 6*E*). The tumor-to-liver ratio of [^{18}F]DMPY2 was more than 4.5- and 7.6-fold higher than that of [^{18}F]P3BZA and [^{18}F]FBZA, respectively ([^{18}F]DMPY2: 10.30 ± 2.22; [^{18}F]P3BZA: 2.25 ± 0.36; [^{18}F]FBZA: 1.35 ± 0.30; $^*P < 0.05$; Fig. 6*F*). When the three tracers were evaluated in lung and LN metastasis models, metastatic lesions were clearly demonstrated on [^{18}F]DMPY2 PET images, whereas the higher background activity of [^{18}F]P3BZA and [^{18}F]FBZA could impede PET imaging (Fig. 6 *G*–*L*).

Discussion

In the present study, we demonstrated the excellent performance of [^{18}F]DMPY2 for detecting primary and metastatic melanomas. The unique properties of [^{18}F]DMPY2 indicate its great potential as a candidate for a theranostic probe, as well as a molecular imaging agent for patients with malignant melanoma.

[^{18}F]DMPY2 may well show much better performance in finding melanoma lesions than the previously reported benzamide derivatives (4, 21–28, 32–34, 36–47) and, in comparison with them, we made two noteworthy structural modifications to improve its biological properties. First, we decreased the alkyl chain of the amine residue from diethyl to dimethyl. Benzamide derivatives such as [^{18}F]FBZA have a diethyl amine residue, and some such compounds with an alkyl (number of carbon: > 3), cycloalkyl, or pyridyl structure in the amine residue showed melanoma uptake of less than 9.0%ID/g at 60 min in B16F10

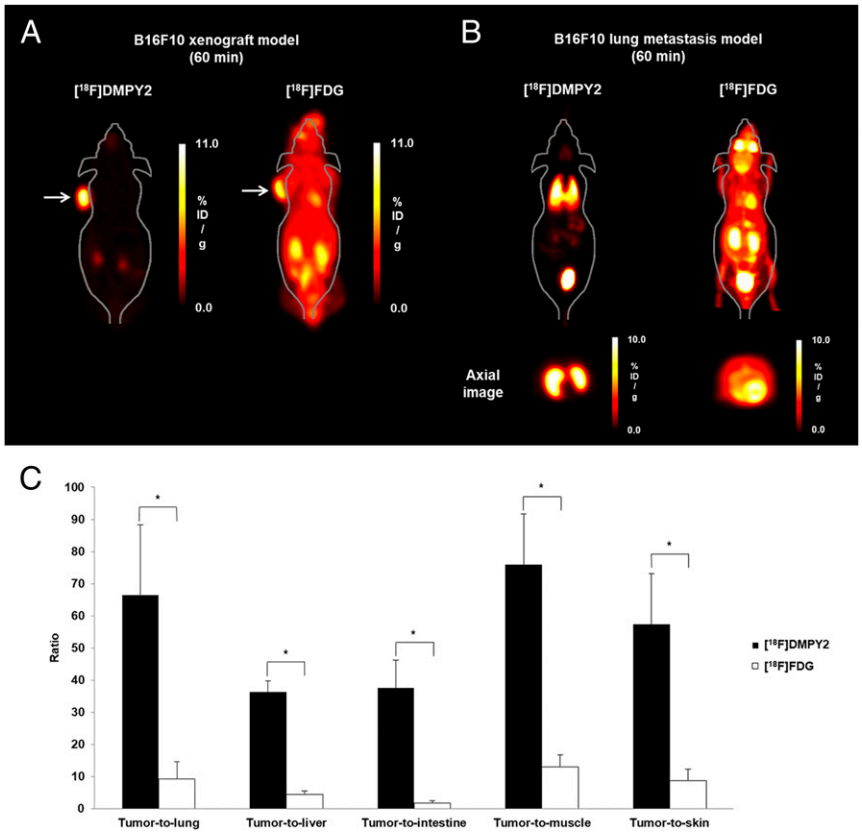

Fig. 5. Head-to-head comparison of [^{18}F]DMPY2 and [^{18}F]FDG in Foxn1nu mice bearing a B16F10 xenograft or lung metastasis. (*A*) Coronal images of B16F10-bearing mice models at 60 min postinjection of radiotracers (*Left*, [^{18}F]DMPY2; *Right*, [^{18}F]FDG; white arrow). (*B*) MIP (*Upper*) and transaxial (*Lower*) image at 60 min postinjection of radiotracers in mice models of lung metastasis. (*C*) s.c. tumor-to-lung, -liver, -intestine, -muscle, and -skin uptake ratios of [^{18}F]DMPY2 and [^{18}F]FDG in a B16F10-bearing mouse at 60 min (*$P < 0.05$).

xenografts. We recently reported [^{18}F]DMFB with an amine residue modified from diethyl to dimethyl, which revealed higher tumor uptake than the unmodified tracer (39). Second, in the present study, we substituted pyridine for benzene in the [^{18}F]DMFB structure, and this modification further increased the tumor uptake up to 24%ID/g in B16F10 xenografts. Therefore, as both the benzene ring and the aliphatic structure are involved in the mechanism of melanin binding, we speculate that the present modifications to the benzene ring and aliphatic structure synergize the target binding activity of [^{18}F]DMPY2 in melanoma and the clearance from normal organs.

The in vivo biodistribution and microPET study revealed that [^{18}F]DMPY2 showed rapid washout from all examined organs, as well as high tumor uptake, resulting in high tumor-to-organ ratios. For example, the tumor-to-liver ratio of [^{18}F]DMPY2 was 11.0- and 14.7-fold higher than that of [^{18}F]P3BZA and [^{18}F]FBZA, respectively. Tumor-to-lung, -liver, -intestine, -bone, -brain, and -skin ratios are important when developing an imaging agent for malignant melanoma because these organs are known to be common sites for metastasis (48). In vivo clearance is related to the hydrophilicity of labeled compounds because lipophilic molecules have a tendency to be metabolized, while hydrophilic molecules tend to be excreted actively or passively (49). The rapid washout of [^{18}F]DMPY2 in comparison with [^{18}F]P3BZA and [^{18}F]FBZA might be attributed to decreased lipophilicity (lowest log *P* value) due to nitrogen in the 3-position of the pyridine ring and dimethyl functional groups in the structure (42, 50–52).

The greater tumoral uptake of [^{18}F]DMPY2 over [^{18}F]DMPY3 might be due to its chemical stability. The 2-position of the pyridine ring of [^{18}F]DMPY3 shows high reactivity toward nucleophilic aromatic substitution, which may decrease its in vivo stability because of certain nucleophiles in the body, including water, amino acid, or proteins. By contrast, the relatively low reactivity of the 3-position of the pyridine ring of [^{18}F]DMPY2 increased its in vivo stability, which may have improved tumor uptake and retention (4).

Another goal of this study was to assess the feasibility of [^{18}F]DMPY2 or [^{18}F]DMPY3 for detection of metastatic melanomas. The present results demonstrate the superior performance of [^{18}F]DMPY2 for detecting metastatic melanoma, including tiny melanin-containing foci, and suggest its strong potential for clinical translation. The uptake value of [^{18}F]DMPY2 was higher than that of [^{18}F]DMPY3 and [^{18}F]FBZA in metastatic lesions, which is consistent with the results on s.c. xenografts. High-resolution autoradiography of metastatic lung slices demonstrated the ability of [^{18}F]DMPY2 to identify small melanoma foci in the tissues. The phosphor imaging scanner detected radioactivity at the microregional level with a spatial resolution of 25 μm. Furthermore, [^{18}F]DMPY2 detected all metastatic LNs and demonstrated clear detection of very tiny LN metastases (<2.0 mm). The LN status near to the primary tumor is a very important prognostic factor for malignant melanoma patients because the lymphatic system is certainly involved in spreading melanoma (53, 54). Once a lymphatic vessel is invaded by melanoma cells, the cells transit through the LN and enter the systemic circulation via the thoracic duct.

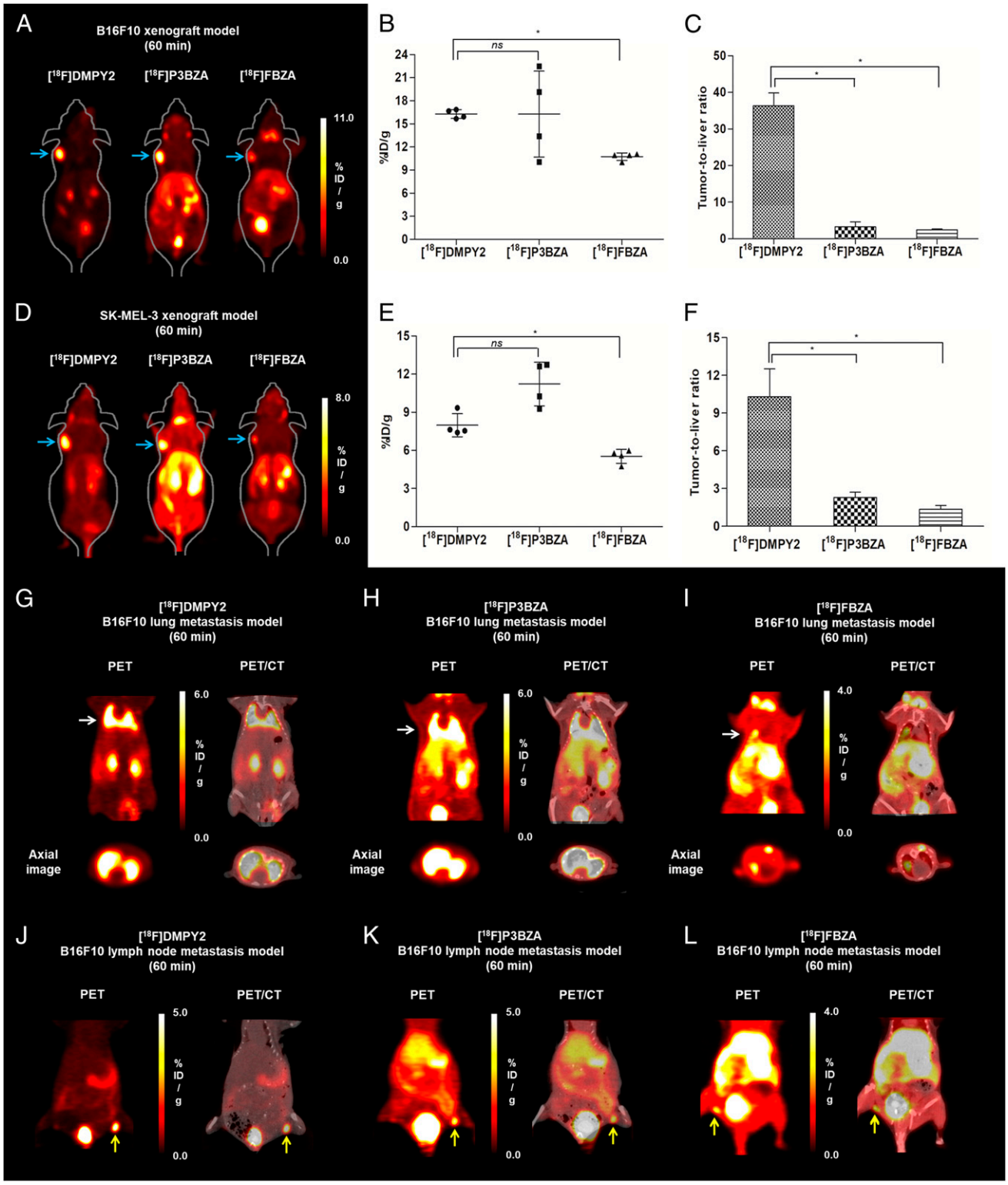

Fig. 6. Head-to-head comparisons of [^{18}F]DMPY2 and [^{18}F]P3BZA or [^{18}F]FBZA in xenograft or metastasis models. (*A*) Representative coronal microPET images of [^{18}F]DMPY2, [^{18}F]P3BZA, or [^{18}F]FBZA at 60 min postinjection in B16F10 xenografts ($n = 4$, 7.4 MBq, each, blue arrow). (*B* and *C*) Tumor uptake values (*B*) and tumor-to-liver ratios (*C*) of [^{18}F]DMPY2, [^{18}F]P3BZA, and [^{18}F]FBZA at 60 min in B16F10 xenografts ($n = 4$, ns = not significant, $*P < 0.05$). (*D*) Representative coronal microPET images at 60 min after i.v. injection of [^{18}F]DMPY2, [^{18}F]P3BZA, and [^{18}F]FBZA in SK-MEL-3 xenografts ($n = 4$, 7.4 MBq, each, blue arrow). (*E* and *F*) Tumor uptake value (*E*) and tumor-to-liver ratios (*F*) of [^{18}F]DMPY2 and [^{18}F]FBZA at 60 min in SK-MEL-3 xenografts ($n = 4$, ns = not significant, $*P < 0.05$). (*G–I*) [^{18}F]DMPY2 (*G*), [^{18}F]P3BZA (*H*), and [^{18}F]FBZA (*I*) imaging in B16F10 lung metastasis (white arrow) mouse models. (*J–L*) [^{18}F]DMPY2 (*J*), [^{18}F]P3BZA (*K*) and [^{18}F]FBZA (*L*) imaging in B16F10 LN metastasis (yellow arrow) mouse models (injection dose: 7.4 MBq, acquisition time: 10 min).

We should point out that the absolute uptake value of [^{18}F]DMPY2 depended on the level of melanin expression; thus [^{18}F]DMPY2 might have low diagnostic accuracy in amelanotic melanoma (AM). However, "true" AM is extremely rare. A review of the literature indicates that AM represents 2–8% of all malignant melanomas, although the precise incidence is difficult to calculate as the term amelanotic is often used to indicate melanomas only partially devoid of pigment. Even in "true" AM, some pigmentation is often present at the periphery of the lesion (55). As shown in microPET studies of weaker-pigmented human melanoma xenografts (SK-MEL-3 and A375-P), [^{18}F]DMPY2 demonstrated tumor uptake with an extremely low background. Therefore, we would still expect [^{18}F]DMPY2 to have diagnostic power in AM patients. Furthermore, it is possible that [^{18}F]DMPY2 provides important information on melanin expression levels, which would be an advantage in the context of theranostics, a close connection between targeted molecular imaging and consequent therapy using radionuclide pairs. The presence and degree of melanin expression will be associated with a therapy response. Thus, [^{18}F]DMPY2 will be introduced as a predictive biomarker.

The field of theranostics is aimed at the targeting, imaging, and treatment of diseases using one chemical structure in which the radioisotope pairs (diagnostic radionuclides/therapeutic counterparts) such as ^{124}I/^{131}I, ^{68}Ga/^{177}Lu, ^{89}Zr/^{90}Y, or ^{64}Cu/^{67}Cu are easily replaceable. Therefore, bifunctional chelators or specific functional groups for radioisotope pairs could be introduced after making appropriate structural modifications that do not perturb the pharmacokinetic benefit of [^{18}F]DMPY2.

In conclusion, [^{18}F]DMPY2 and [^{18}F]DMPY3 were easily synthesized via a simple nucleophilic substitution reaction. Both of the pyridine-based benzamide derivatives [^{18}F]DMPY2 and [^{18}F]DMPY3 showed excellent performance in detecting melanoma cells. The specific/rapid targeting, prolonged retention, and rapid clearance of [^{18}F]DMPY2 in primary and metastatic tumors suggests that this radiotracer could be used as a PET imaging agent to obtain outstanding image quality in the diagnosis of melanoma. The excellent characteristics of [^{18}F]DMPY2 warrant its further investigation for clinical translation and theranostic approaches.

Materials and Methods

Additional details on the synthesis of reference compounds and precursors, stability study, cell culture, cellular uptake studies, preparation of animal models, and high-resolution autoradiography are given in *SI Appendix, Methods*.

Radiolabeling of [^{18}F]DMPY2 and [^{18}F]DMPY3. [^{18}F]Fluoride was eluted by aqueous potassium carbonate (K_2CO_3) into a vial and dried with Kryptofix 2.2.2 in acetonitrile by nitrogen gas at 90 °C. The solution was dried two times more with acetonitrile by azeotropic distillation. Then, the precursor (5 mg) dissolved in *N,N*-dimethyl sulfoxide (DMSO; 200 μL) was added to the vial. The reaction mixture was heated at 120 °C for 15 min and then cooled. The solution was injected into a semipreparative HPLC column system for purification (Column: Phenomenex Luna C18, 250 × 10.0 mm; ultraviolet: 254 nm). [^{18}F]DMPY2: The mobile phase started with 100% solvent A (0.1% trifluoroacetic acid in water) and 0% solvent B (0.1% trifluoroacetic acid in acetonitrile), and increased to 40% solvent A and 60% solvent B at 30 min; flow rate = 3 mL/min (retention time [R_t]: 19.49 min). [^{18}F]DMPY3: The mobile phase started with 100% solvent A and 0% solvent B and increased to 30% solvent A and 70% solvent B at 30 min; flow rate = 3 mL/min [R_t: 19.77 min].

Biodistribution Studies. Animal care, animal experiments, and euthanasia were performed in accordance with protocols approved by the Chonnam National University Animal Research Committee and the Guide for the Care and Use of Laboratory Animals. The biodistribution studies were performed 10, 30, and 60 min after i.v. injection of 7.4 MBq of [^{18}F]DMPY2 and [^{18}F]DMPY3 into B16F10 s.c. tumor models. Tumor, blood, and other organs were extracted and weighed, and the radioactivity in the organs was counted using a gamma counter. To obtain the %ID/g, radioactivity determinations were normalized against the weight of tissue and the amount of radioactivity injected.

Small Animal PET. MicroPET images were obtained using a high-resolution small animal PET-SPECT-CT scanner (Inveon, Siemens Medical Solutions). MicroPET studies of the tumor models (tumor size: 80–120 mm^3) were performed after i.v. injection of [^{18}F]DMPY2, [^{18}F]DMPY3, [^{18}F]FDG, [^{18}F]P3BZA, or [^{18}F]FBZA (7.4 MBq), with images being acquired for 10 min. Head-to-head comparison of radiotracers were performed in the same mouse models bearing xenograft, lung metastasis, or LN metastasis. One day after [^{18}F]FDG, [^{18}F]P3BZA, or [^{18}F]FBZA PET imaging, the same mice were injected with [^{18}F]DMPY2 or [^{18}F]DMPY3. ROI were drawn over blood, heart, lung, liver, intestine, kidney, muscle, bone, brain, bladder, skin, and primary or metastatic tumors on decay-corrected coronal images, and the maximum %ID/g values were measured (%ID/g_{max}). The acquired images were reconstructed with a three-dimensional ordered subset expectation maximization (OSEM3D) algorithm, and image analysis was performed with PMOD software (PMOD Technologies Ltd.). Uptake values are expressed as %ID/g for coronal and transaxial PET images.

Statistical Analysis. Statistical analysis was performed as described using the GraphPad Prism 8.0 software (GraphPad Software, Inc.). Statistical differences were measured using the Mann–Whitney *U* test. A *P* value of <0.05 was considered statistically significant. All data are expressed as the mean ± SD.

Data Availability. All data, associated synthesis, methods, and materials can be accessed in the text or *SI Appendix*.

ACKNOWLEDGMENTS. We thank Hwa Youn Jang (Innovation Center for Molecular Probe Development) for his excellent research assistance. This research was supported by the Pioneer Research Center Program through the National Research Foundation of Korea, funded by the Ministry of Science and Information & Communication Technology Grant 2015M3C1A3056410, and by the Basic Science Research Program through the National Research Foundation of Korea, funded by Ministry of Education Grants 2017R1D1A1B03029055 and 2018R1A6A3A01012344.

1. M. Harries *et al*., Treatment patterns of advanced malignant melanoma (stage III-IV)–A review of current standards in Europe. *Eur. J. Cancer* **60**, 179–189 (2016).
2. C. Garbe *et al*.; European Dermatology Forum (EDF); European Association of Dermato-Oncology (EADO); European Organisation for Research and Treatment of Cancer (EORTC), Diagnosis and treatment of melanoma. European consensus-based interdisciplinary guideline–Update 2016. *Eur. J. Cancer* **63**, 201–217 (2016).
3. V. Henriques, T. Martins, W. Link, B. I. Ferreira, The emerging therapeutic landscape of advanced melanoma. *Curr. Pharm. Des.* **24**, 549–558 (2018).
4. H. Liu *et al*., Development of ^{18}F-labeled picolinamide probes for PET imaging of malignant melanoma. *J. Med. Chem.* **56**, 895–901 (2013).
5. T. Z. Belhocine, A. M. Scott, E. Even-Sapir, J. L. Urbain, R. Essner, Role of nuclear medicine in the management of cutaneous malignant melanoma. *J. Nucl. Med.* **47**, 957–967 (2006).
6. R. S. Prichard, A. D. Hill, S. J. Skehan, N. J. O'Higgins, Positron emission tomography for staging and management of malignant melanoma. *Br. J. Surg.* **89**, 389–396 (2002).
7. B. Krug *et al*., Role of PET in the initial staging of cutaneous malignant melanoma: Systematic review. *Radiology* **249**, 836–844 (2008).
8. A. Dimitrakopoulou-Strauss, L. G. Strauss, C. Burger, Quantitative PET studies in pretreated melanoma patients: A comparison of 6-[^{18}F]fluoro-L-dopa with ^{18}F-FDG and (^{15})O-water using compartment and noncompartment analysis. *J. Nucl. Med.* **42**, 248–256 (2001).
9. P. Lindholm *et al*., Carbon-11-methionine PET imaging of malignant melanoma. *J. Nucl. Med.* **36**, 1806–1810 (1995).
10. D. C. Cobben *et al*., 3′-18F-fluoro-3′-deoxy-L-thymidine: A new tracer for staging metastatic melanoma? *J. Nucl. Med.* **44**, 1927–1932 (2003).
11. R. Haubner *et al*., Noninvasive visualization of the activated alphavbeta3 integrin in cancer patients by positron emission tomography and [^{18}F]Galacto-RGD. *PLoS Med.* **2**, e70 (2005).
12. E. A. Choi, J. E. Gershenwald, Imaging studies in patients with melanoma. *Surg. Oncol. Clin. N. Am.* **16**, 403–430 (2007).
13. A. L. Vavere *et al*., ^{64}Cu-*p*-NH_2-Bn-DOTA-hu14.18K322A, a PET radiotracer targeting neuroblastoma and melanoma. *J. Nucl. Med.* **53**, 1772–1778 (2012).
14. S. D. Voss *et al*., Positron emission tomography (PET) imaging of neuroblastoma and melanoma with ^{64}Cu-SarAr immunoconjugates. *Proc. Natl. Acad. Sci. U.S.A.* **104**, 17489–17493 (2007).
15. J. Yang *et al*., ^{68}Ga-DOTA-GGNle-CycMSH$_{hex}$ targets the melanocortin-1 receptor for melanoma imaging. *Sci. Transl. Med.* **10**, eaau4445 (2018).
16. N. K. Tafreshi *et al*., Synthesis and characterization of a melanoma-targeted fluorescence imaging probe by conjugation of a melanocortin 1 receptor (MC1R) specific ligand. *Bioconjug. Chem.* **23**, 2451–2459 (2012).

17. N. M. Barkey *et al*., Development of melanoma-targeted polymer micelles by conjugation of a melanocortin 1 receptor (MC1R) specific ligand. *J. Med. Chem.* **54**, 8078–8084 (2011).
18. C. Zhang *et al*., Preclinical melanoma imaging with ^{68}Ga-labeled α-melanocyte-stimulating hormone derivatives using PET. *Theranostics* **7**, 805–813 (2017).
19. J. Xu, J. Yang, Y. Miao, Dual receptor-targeting ^{99}mTc-labeled Arg-Gly-Asp-conjugated Alpha-Melanocyte stimulating hormone hybrid peptides for human melanoma imaging. *Nucl. Med. Biol.* **42**, 369–374 (2015).
20. H. Guo, F. Gallazzi, Y. Miao, Design and evaluation of new Tc-99m-labeled lactam bridge-cyclized alpha-MSH peptides for melanoma imaging. *Mol. Pharm.* **10**, 1400–1408 (2013).
21. H. J. Kim *et al*., Synthesis and evaluation of a novel ^{68}Ga-labeled DOTA-benzamide derivative for malignant melanoma imaging. *Bioorg. Med. Chem. Lett.* **22**, 5288–5292 (2012).
22. H. J. Kim *et al*., Synthesis and characterization of a (^{68})Ga-labeled N-(2-diethylaminoethyl)benzamide derivative as potential PET probe for malignant melanoma. *Bioorg. Med. Chem.* **20**, 4915–4920 (2012).
23. G. Ren *et al*., Melanin-targeted preclinical PET imaging of melanoma metastasis. *J. Nucl. Med.* **50**, 1692–1699 (2009).
24. S. Garg, K. Kothari, S. R. Thopate, A. K. Doke, P. K. Garg, Design, synthesis, and preliminary in vitro and in vivo evaluation of N-(2-diethylaminoethyl)-4-[^{18}F]fluorobenzamide ([^{18}F]-DAFBA): A novel potential PET probe to image melanoma tumors. *Bioconjug. Chem.* **20**, 583–590 (2009).
25. P. Auzeloux, J. Papon, R. Pasqualini, J. C. Madelmont, Synthesis and biodistribution of a new oxo-technetium-99m bis(aminothiol) complex as a potential melanoma tracer. *J. Med. Chem.* **44**, 1116–1121 (2001).
26. P. Auzeloux *et al*., A potential melanoma tracer: Synthesis, radiolabeling, and biodistribution in mice of a new nitridotechnetium bis(aminothiol) derivative pharmacomodulated by a N-(diethylaminoethyl)benzamide. *J. Med. Chem.* **43**, 190–198 (2000).
27. P. Auzeloux *et al*., Synthesis and biodistribution of technetium-99m-labelled N-(diethylaminoethyl)benzamide via a bis(dithiocarbamate) nitridotechnetiuim(V) complex. *J. Labelled Compd. Rad.* **42**, 325–335 (1999).
28. P. Auzeloux *et al*., Technetium-99m radiolabelling of an N-amino-alkyl-benzamide nitrido- and oxo-technetium bis(aminoethanethiol) derivative synthesis and biological results. Potential melanoma tracer agents. *J. Labelled Compd. Rad.* **42**, 567–579 (1999).
29. C. Nicholl, A. Mohammed, W. E. Hull, B. Bubeck, M. Eisenhut, Pharmacokinetics of iodine-123-IMBA for melanoma imaging. *J. Nucl. Med.* **38**, 127–133 (1997).
30. L. Maffioli *et al*., Scintigraphic detection of melanoma metastases with a radiolabeled benzamide ([iodine-123]-(S)-IBZM). *J. Nucl. Med.* **35**, 1741–1747 (1994).
31. J. M. Michelot *et al*., Phase II scintigraphic clinical trial of malignant melanoma and metastases with iodine-123-N-(2-diethylaminoethyl 4-iodobenzamide). *J. Nucl. Med.* **34**, 1260–1266 (1993).
32. G. Trencsényi *et al*., Comparative preclinical evaluation of ^{68}Ga-NODAGA and ^{68}Ga-HBED-CC conjugated procainamide in melanoma imaging. *J. Pharm. Biomed. Anal.* **139**, 54–64 (2017).
33. I. Kertész *et al*., In vivo imaging of experimental melanoma tumors using the novel tadiotracer ^{68}Ga-NODAGA-Procainamide (PCA). *J. Cancer* **8**, 774–785 (2017).
34. C. C. Chang *et al*., Preparation and characterization of a novel Al(^{18})F-NOTA-BZA conjugate for melanin-targeted imaging of malignant melanoma. *Bioorg. Med. Chem. Lett.* **26**, 4133–4139 (2016).
35. X. Ma *et al*., Biodistribution, radiation dosimetry, and clinical application of a melanin-targeted PET probe, ^{18}F-P3BZA, in patients. *J. Nucl. Med.* **60**, 16–22 (2019).
36. S. Y. Wu *et al*., Synthesis and preclinical characterization of [^{18}F]FPBZA: A novel PET probe for melanoma. *BioMed Res. Int.* **2014**, 912498 (2014).
37. D. Denoyer *et al*., High-contrast PET of melanoma using (^{18})F-MEL050, a selective probe for melanin with predominantly renal clearance. *J. Nucl. Med.* **51**, 441–447 (2010).
38. H. Liu *et al*., A novel aliphatic 18F-labeled probe for PET imaging of melanoma. *Mol. Pharm.* **10**, 3384–3391 (2013).
39. A. Pyo *et al*., N-(2-(dimethylamino)ethyl)-4-^{18}F-fluorobenzamide: A novel molecular probe for high-contrast PET imaging of malignant melanoma. *J. Nucl. Med.* **60**, 924–929 (2019).
40. H. Feng *et al*., Imaging malignant melanoma with (^{18})F-5-FPN. *Eur. J. Nucl. Med. Mol. Imaging* **43**, 113–122 (2016).
41. L. Rbah-Vidal *et al*., Early detection and longitudinal monitoring of experimental primary and disseminated melanoma using [^{10}F]ICF01006, a highly promising melanoma PET tracer. *Eur. J. Nucl. Med. Mol. Imaging* **39**, 1449–1461 (2012).
42. I. Greguric *et al*., Discovery of [^{18}F]N-(2-(diethylamino)ethyl)-6-fluoronicotinamide: A melanoma positron emission tomography imaging radiotracer with high tumor to body contrast ratio and rapid renal clearance. *J. Med. Chem.* **52**, 5299–5302 (2009).
43. Z. Cheng, A. Mahmood, H. Li, A. Davison, A. G. Jones, [^{99m}TcOAADT]-$(CH_2)_2$-NEt_2: A potential small-molecule single-photon emission computed tomography probe for imaging metastatic melanoma. *Cancer Res.* **65**, 4979–4986 (2005).
44. M. Eisenhut *et al*., Melanoma uptake of (^{99m})Tc complexes containing the N-(2-diethylaminoethyl)benzamide structural element. *J. Med. Chem.* **45**, 5802–5805 (2002).
45. J. M. Michelot *et al*., Synthesis and evaluation of new iodine-125 radiopharmaceuticals as potential tracers for malignant melanoma. *J. Nucl. Med.* **32**, 1573–1580 (1991).
46. C. C. Chang *et al*., Synthesis and characterization of a novel radioiodinated phenylacetamide and its homolog as theranostic agents for malignant melanoma. *Eur. J. Pharm. Sci.* **81**, 201–209 (2016).
47. X. Liu *et al*., Synthesis and evaluation of novel radioiodinated nicotinamides for malignant melanoma. *Nucl. Med. Biol.* **35**, 769–781 (2008).
48. W. E. Damsky, L. E. Rosenbaum, M. Bosenberg, Decoding melanoma metastasis. *Cancers (Basel)* **3**, 126–163 (2010).
49. D. A. Smith, K. Beaumont, T. S. Maurer, L. Di, Clearance in drug design. *J. Med. Chem.* **62**, 2245–2255 (2019).
50. B. Jeffries *et al*., Reducing the lipophilicity of perfluoroalkyl groups by CF_2-F/CF_2-Me or CF_3/CH_3 exchange. *J. Med. Chem.* **61**, 10602–10618 (2018).
51. D. Y. Kim *et al*., Comparison of ^{18}F-labeled fluoroalkylphosphonium cations with ^{13}N-NH_3 for PET myocardial perfusion imaging. *J. Nucl. Med.* **56**, 1581–1586 (2015).
52. K. D. Freeman-Cook, R. L. Hoffman, T. W. Johnson, Lipophilic efficiency: The most important efficiency metric in medicinal chemistry. *Future Med. Chem.* **5**, 113–115 (2013).
53. S. Pasquali *et al*., Early (sentinel lymph node biopsy-guided) versus delayed lymphadenectomy in melanoma patients with lymph node metastases: Personal experience and literature meta-analysis. *Cancer* **116**, 1201–1209 (2010).
54. J. M. Thomas, Sentinel lymph node biopsy in malignant melanoma. *BMJ* **336**, 902–903 (2008).
55. M. A. Pizzichetta *et al*., Amelanotic/hypomelanotic melanoma: Clinical and dermoscopic features. *Br. J. Dermatol.* **150**, 1117–1124 (2004).